ADVANCED MATERIALS INTERFACES
Open Access
www.advmatinterfaces.de

Efficient Optimization of High-Quality Epitaxial Lithium Niobate Thin Films by Chemical Beam Vapor Deposition: Impact of Cationic Stoichiometry

Anna L. Pellegrino, Estelle Wagner, Francesca Lo Presti, William Maudez, Simon Kolb, Rashmi Rani, Antoine Bernard, Stephan Guy, Alban Gassenq, Marina Raevskaia, Christian Grillet, Rahma Moalla, Claude Botella, Romain Bachelet, Bruno Masenelli, Jean-Marie Bluet, Sebastien Cueff, Patrick Chapon, Giacomo Benvenuti, and Graziella Malandrino**

Lithium niobate is a material of special interest for its challenging functional properties, which can suit various applications. However, high quality 200-mm $Li_xNb_{1-x}O_3$ thin film grown on sapphire substrate have never been reported so far which limits these potential applications. This paper reports the efficient optimization of high quality $LiNbO_3$ thin film deposition on sapphire (001) substrate through chemical beam vapor deposition in a combinatorial configuration. With this technique, flow ratio of Li/Nb can be tuned from ≈0.25 to ≈2.45 on a single wafer. Various complementary characterizations (by means of diffraction, microscopy and spectroscopy techniques) have been performed at different areas of the film (different cationic ratios) in order to investigate the impact of the cationic stoichiometry deviation on the film properties. Close to cationic stoichiometry ($LiNbO_3$), the epitaxial films are of high quality (single phase in spite of two in-plane domains, low mosaicity of 0.04°, low surface roughness, refractive index and band gap close to bulk values). Deviating from the stoichiometry conditions, secondary phases are detected ($LiNb_3O_8$ for Nb-rich flow ratios, and Li_3NbO_4 with partial amorphization for Li-rich flow ratios). $LiNbO_3$ films are of high interest for various key applications in data communications among others.

1. Introduction

Lithium niobate ($LiNbO_3$, LNO) is a synthetic material composed of niobium, lithium and oxygen, which is piezoelectric and ferroelectric, and possesses excellent electro-optic and non-linear optical properties.[1–3] The research on LNO has been the focus of several studies around the seventies due to its important application for the development of surface acoustic wave (SAW) devices and, in the market of single-crystalline piezoelectrics, it has taken second place only to quartz.[4,5] Today, SAW devices are applied as radio-frequency filters, of which 70% are fabricated on LNO single crystals.[6] In addition, its study has raised more and more attention as LNO-on-insulator platform, as a promising candidate for integrated high-performance modulators and integrated on-chip micro-photonic devices.[7–9] LNO

A. L. Pellegrino, F. Lo Presti, G. Malandrino
Dipartimento di Scienze Chimiche
Università di Catania and INSTM UdR Catania
Catania 95125, Italy
E-mail: gmalandrino@unict.it

E. Wagner, W. Maudez, S. Kolb, R. Rani, R. Moalla, G. Benvenuti
3D-Oxides
St Genis Pouilly 01630, France
E-mail: giacomo.benvenuti@3d-oxides.com

The ORCID identification number(s) for the author(s) of this article can be found under https://doi.org/10.1002/admi.202300535

DOI: 10.1002/admi.202300535

E. Wagner, W. Maudez, S. Kolb, R. Rani, G. Benvenuti
ABCD Technology
Nyon 1260, Switzerland

A. Bernard, S. Guy, A. Gassenq
Institute Light Matter ILM – UMR5306, Univ Lyon 1
CNRS
Villeurbanne, Cedex 69622, France

M. Raevskaia, C. Grillet, R. Moalla, C. Botella, R. Bachelet, B. Masenelli, J.-M. Bluet, S. Cueff
Institut des Nanotechnologies de Lyon INL – Univ Lyon
CNRS, ECL, INSA Lyon, UCBL
CPE
Ecully Cedex 69134, France

P. Chapon
HORIBA France
Bd Thomas Gobert
Palaiseau 91120, France

also plays a pivotal role in photonics, similar to the role played by silicon in electronics, and for this reason LNO has been dubbed as "the silicon of photonics".[10] Several of the above-mentioned industrial applications could be boosted by the fabrication of high quality LNO films, for example epitaxial films are desired for electro-optic and non-linear optical applications,[11] and acoustic devices.[12b,13] The challenge to deposit such films includes not only the capability to control material stoichiometry and crystalline quality, but also the possibility to deposit films of the required thicknesses (typically hundreds of nm for optical devices and micrometers for acoustic devices) with growth rates and production volume compatible with industrial applications. If a lot of research has focused on this goal over the last 50 years and lots of progresses have been made, the quest for the holy grail is not yet over, as pointed at in the recent review of Zivasatienraj et al.[11] For applications, there is also actually a huge interest in being able to deposit high quality LNO films on non-epitaxial substrates, in particular on silicon.[14–16] In all cases, the nature of the substrate or of the buffer-layer on which the film is grown plays a critical role for the film quality, with desired crystalline-domain orientations depending on applications and devices.[17] Thus, for pyroelectric, piezoelectric, and some electro-optic applications, *c*-axis oriented LNO are generally preferred,[12a] while a-axis (in-plane) domain orientations are desired for the acoustic and optical applications.[12b] LNO belongs to the trigonal crystal system, with threefold rotational symmetry around the *c*-axis in a hexagonal symmetry (R3c space group, 3m point group). Sapphire has a similar structure with comparable lattice constants (nearly 8% in-plane mismatch in compression),[18] that makes it a good substrate for *c*-axis oriented LNO epitaxial growth. Additionally, LNO has an optical index significantly higher than sapphire (2.2-2.3 to be compared with 1.75-1.76), which makes again sapphire an interesting substrate for optical waveguiding applications. However, growing high quality epitaxial stoichiometric LNO films is still challenging.

One reason of the difficulty in growing high quality LNO films is that LNO has no "chemical-line composition" that would thermodynamically favor its formation, but it can exist over a narrow composition range around the stoichiometry Li/Nb = 1,[19] and the functional properties rapidly diverge as composition changes. Therefore, extreme limits must be achieved in the control of the required amounts for Nb and Li elements in the deposition technique. As a consequence, if epitaxial LNO thin films have been grown by different techniques ([13] and references therein]), including Liquid phase Epitaxy (LPE),[20] sputtering,[21] Chemical Vapor Deposition (CVD),[22,23] Pulse Laser Deposition (PLD),[24] Molecular Beam Epitaxy (MBE),[25] sol-gel,[26] and atomic layer deposition (ALD),[27] a fabrication approach that allows a precise tuning of the Li and Nb elements, yielding films of high epitaxial quality, is of particular interest for an actual industrial implementation of the LNO films through a potentially appealing technique.

Chemical Beam Vapor Deposition (CBVD) is a thin film deposition technique merging the assets of the more classical Metalorganic Chemical Vapor deposition (MOCVD) and MBE {one of the Chemical Beam Epitaxy (CBE), Metalorganic Molecular Beam Epitaxy (MOMBE), Gas phase Molecular Beam Epitaxy[28] or High-Vacuum Chemical Beam Vapor Deposition (HV-CVD)[29] variants}. As in MBE, it offers a unique control of precursor flow on the substrate with line-of sight trajectories in high vacuum conditions of precursor elements/molecules from sources to substrate, and as in MOCVD, it relies on thermally induced precursor decomposition/adsorption and surface diffusion to form the crystalline film on the heated substrate. More than 10 years ago, LNO deposition on sapphire substrate was already demonstrated by CBVD[18,30] and achieved results are still mentioned as promising in recent reviews.[13] Due to the renewed interest in LNO thin films for various key applications, efforts are done to grow high-quality epitaxial LNO films, as well as new studies on structure-property relationships.

In the present work, combinatorial growth is investigated in an improved CBVD equipment able to yield clear straight lines corresponding to the different Li/Nb ratio. The resulting LNO thin film, having a large lateral composition gradient, has been epitaxially-grown on c-cut sapphire substrate within a single deposition. The film has been fully characterized by various complementary techniques, proving that film composition can be precisely tuned from Nb rich phases, to stoichiometric, to Li rich phases, inducing variation of crystalline quality and optical properties. A major problem dealing with LNO film characterization is to probe the exact chemical composition of LNO films, being Li a very light element and consequently not quantifiable with classical quantitative analyses. Thus, the Li/Nb ratio is usually evaluated through indirect techniques such as Raman and X-ray diffraction (XRD). Comparing with these techniques, rf-Glow Discharge Emission Spectroscopy (rf-GDOES)[31] has been applied for the first time, to our knowledge, as a very rapid and efficient way of screening film composition as a function of Li/Nb ratio. rf-GDOES is demonstrated as an easy to handle, high throughput characterization technique to map rapidly film composition on a combinatorial sample. In addition, an in-depth characterization of the LNO films has been carried out, for each given significant composition, using field emission scanning electron microscopy (FE-SEM), atomic force microscopy (AFM), XRD and Raman spectroscopy that are known as valuable indirect techniques[12] to evaluate LNO film quality. Optical index and band gap measurements have been carried out through UV-vis spectroscopy and ellipsometry. Finally, M line investigation has proven that such $LiNbO_3$ thin films should support low-loss guided optical modes, thus enabling to go one step further towards a practical use of the layers in optical applications.

2. Results

Lithium niobate films have been deposited through a combinatorial CBVD from the lithium tert-butoxide (hexameric in the vapor phase, $[Li(O^tBu)]_6$) and niobium tetraethoxide dimethylaminoethoxide $[Nb(OEt)_4dmae]$ precursors, whose schemes are reported in **Figure 1**. The advantage of a combinatorial process is that it allows within a single deposition run to strictly evaluate the variation of flow as a function of the position on the substrate, keeping all other parameters identical. In this study, a special type of CBVD equipment, developed for more than 20 years by ABCD Technology,[32–36] has been used. It shows unique advantages of uniform deposition over large substrates (currently 450 mm wafer with ± 5% film homogeneity) of complex materials (up to 5 precursors can be introduced simultaneously and independently in recent Sybilla equipment[32]), with efficient combinatorial

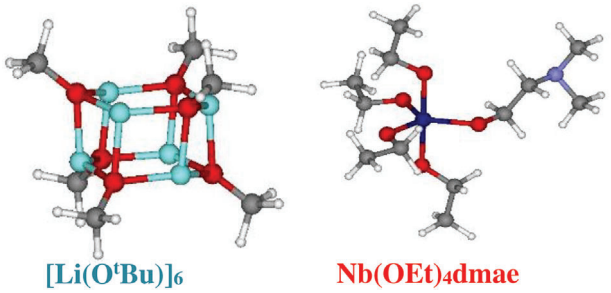

Figure 1. Model structures of lithium and niobium precursors.

configurations[33] and compatibility with additive growth depositing through shadow masks,[37] over wide growth rate ranges (from few tens of nm/hour up to 20 µm h^{-1}).

Deposition conditions have been selected adjusting pre-chamber vapor pressures varying reservoir temperature according to calibration vapor tension curves presented in **Figure 2**.

Specifically, the pre-chamber vapor pressures of both lithium and niobium precursors measured with 6 active sources per line as a function of reservoir temperature are reported on the right. Arrhenius law is found, with an apparent enthalpy of evaporation of 59.0 ± 7.4 kJ mol^{-1} for $[Li(O^tBu)]_6$ and 75.4 ± 4.0 kJ mol^{-1} for $Nb(OEt)_4$dmae over the measured temperature range of 20 °C. The reservoir temperatures and measured pre-chamber pressures used in the considered deposition conditions are presented as diamond points: values differ slightly from calibration curves because deposition conditions include 3 open sources instead of 6, and measurement in the system is not at thermodynamic equilibrium. The present measurements are in good agreement with literature plotted data from Saulys[38] for $[Li(O^tBu)]_6$ and from Dabirian[34] for $Nb(OEt)_4$dmae.

In the combinatorial configuration chosen in this study, the precursor flow ratio varies continuously over the substrate. Values of Li/Nb from 0.25 to 2.45 have been calculated (see **Figure 3**) through flow simulations, carried out based on measured vapor pressure in pre-chambers, according to model detailed in ref.,[33] with slight modification based on calibrations and assuming that both precursors evaporate molecularly, although for $[Li(O^tBu)]_6$, the hexameric structure has been reported in vapor phase.[39]

The resulting thin film exhibits different zones (labelled Z1 to Z6), visible with the naked eye, that correlate well in shape with variation of flow composition of Li/Nb precursor ratio as shown in Figure 3.

2.1. Morphological Characterization

The sample characterization has been carried along the entire substrate (4 inch in diameter), the deposited sapphire wafer was cut in different pieces (labelled Ci) to carry out characterization as indicated in Figure S1 (Supporting Information).

Morphological and topographic characterization of Z1 to Z4 from sample piece C1 has been carried out by optical microscopy (Figure S2, Supporting Information), FE-SEM plan views (**Figure 4**a), FE-SEM cross-sections (Figure 4b), and AFM images (Figure 4c).

Figure S2 (Supporting Information) presents the top view measured by optical microscopy. In zones Z1 to Z3, deposited surfaces observed by optical microscopy, reveal hundreds of micron size domains with three main border orientations that remind the three directions of the hexagonal unit cell perpendicular of *c*-axis oriented LNO crystal (and sapphire substrate).[14] Domain borders are visible, that are typical of well crystalline LNO.[40,41,13]

SEM plan view images in Figure 4a display the formation of homogenous and compact films along all the different zones. In particular, the morphology of Z1 appears nanostructured with grains of dimension of the order of 100 nm. The nanostructured features evolve into smoother surfaces for the Z2 and Z3 regions, which present grains of ≈80–100 nm for the Z2 and barely visible grains in the Z3. Differently, the Z4 zone displays the formation of lamellar like structure with triangular shapes, following the crystallographic axis. Moreover, FE-SEM cross-sectional images in Figure 4b allow to estimate the thickness of the films as a function of the different regions. Specifically, the thickness reaches the highest value of ≈390 nm in the Z1, followed by a slight decrease down to 320 nm for the Z2 zone. Then, a thickness of ≈280–290 nm is assessed in the Z3 and Z4. This trend can be rationalized considering that on increasing Li/Nb from Z1 to Z4 (Li/Nb from ≈0.3 to 0.8) induces a decrease of the film thickness of ≈25% (growth rate reduced from 99 nm h^{-1} to 73 nm h^{-1}).

Finally, the atomic force microscopy (AFM) characterization (Figure 4c) of the four zones confirms as well the homogeneity of the layers with coalesced grains on larger area of 10 µm × 10 µm to 100 µm × 100 µm, and a root mean square (RMS) roughness of ≈3.69 nm, 1.74 nm, and 4.02 nm (measured on areas of 5 µm × 5 µm) for Z1, Z2, and Z3, respectively. In the region Z4 finally, the RMS roughness reaches the value of 40.20 nm, in good correlation with the different morphology observed by FE-SEM.

2.2. Compositional Characterization

Radiofrequency glow discharge (rf-GD) coupled to optical emission spectrometry (OES) has proven to be a useful technique to perform depth profiling studies on thin films.[31] Elemental composition information of the $LiNbO_3$ sample has been derived through rf-GDOES on 11 points on piece C4 (whose positions are shown in **Figure 5**a), with Li precursor flow increasing and Nb precursor flow decreasing from point P1 to point P11 (see flow calculation in Figure 5b). A typical rf-GDOES spectrum for these measurements is presented in Figure 5c, in comparison to a reference spectrum taken on a bulk LNO crystal (from University Wafer[42]). The measured intensities for the different elements are presented as a function of the erosion time (Figure S3, Supporting Information). For the first 4–7 s, a surface contamination layer is observed, rich in Li, O, and C. Then the signals Li, Nb and O stabilize within the deposited films, proving that the film composition is homogenous in depth. The oscillations on the signals are due to optical interference effects of the laser in the transparent film. At the film substrate interface, organometallic contamination is present, with organic C and H peaks observed. This organic contamination could either be due to contamination of the sapphire substrate prior to deposition, or to the formation of organic contamination during the film nucleation phase. Finally,

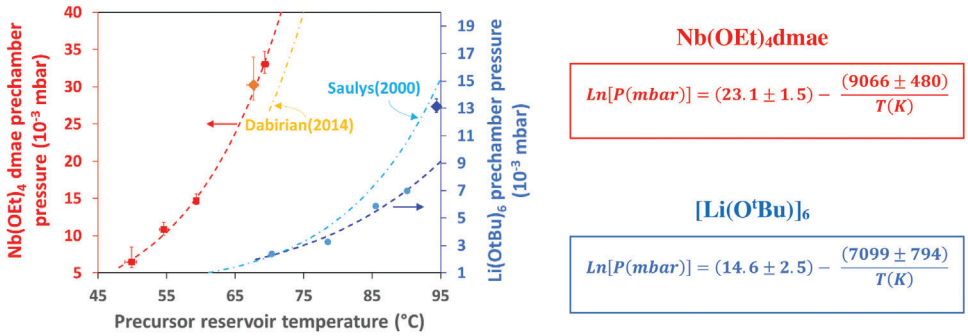

Figure 2. Pre-chamber vapor pressures of both precursors measured with 6 active sources per line as a function of the reservoir temperature (red square, Arrhenius equation of vapor pressure in red for Nb on left y scale, and blue dots, Arrhenius equation of vapor pressure in blue for Li on right y-scale), in comparison to literature data (Darbirian,[34] Saulys[38]). Diamond points correspond to deposition conditions with 3 precursor sources on each line used for the sample characterized in the present work. On the right, equations of pre-chamber vapor pressures of both lithium and niobium precursors are reported.

the Al and O signals deriving from the sapphire substrates are observed. In Figure 5d it is reported the comparison of the Al signal (from the sapphire substrate) and the Nb signal (from the film) in the measurement time range corresponding to the transition from film to substrate.

Calibration shows that the film signals for Li, Nb, and O are 68% of the corresponding signals for the bulk single crystal: this might be explained by variation in the substrate thickness that plays a role in rf coupling.[43]

Considering the signal ratio within the film (taken in the measurement time range typically 10 to 40 s, see **Figure 6**a), it is observed that the Li/Nb signal increases from P1 to P11 (of a factor 2.5, about half of the variation of the precursor flow ratio) starting at P1 from a value similar to the one measured on the bulk LNO (Figure 6a). The O/Li signal ratio decreases from P1 to P11 (of a factor 2 approximately), again with a value at P1 close to the one measured on the bulk LNO (Figure 6b). The C/Li signal ratio decreases with increasing erosion time with a value that surrounds the bulk LNO value, suggesting it is essentially due to surface contamination (but also clearly decreasing from P1 to P11) (Figure 6c). If we compare the decrease of the Nb signal and the increase of the Al signal at the film to substrate interface, it can be clearly shown that the erosion time decreases from P1 to P11 of about 30%. If we compare P5-P6 (in Z4) to P1 (in Z1/Z2), the erosion time is reduced by 12–13% which is in good agreement with film thickness measurements of Figure 4 (280 nm in Z4, 320 nm in Z2 and 390 nm in Z1).

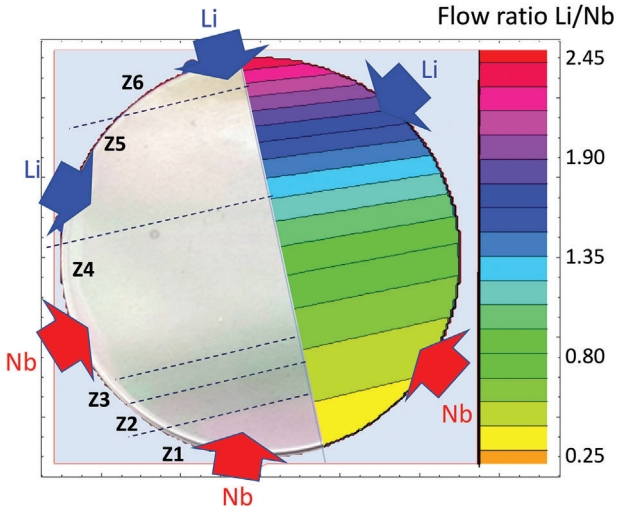

Figure 3. Photograph of the deposited 4-inch wafer on the half-left part in relation to calculated Li/Nb flow ratio on the half-right part (values on right scale). The deposited sample shows 6 areas with very clear boundaries that can be seen with naked eyes are observed (labelled Z1 to Z6), whose borders are indicated by dashed lines.

To complete compositional characterization, surface XPS measurements have been performed at the surface region of samples Z1-Z4 (piece C2). Figure S4 (Supporting Information) presents the XPS spectra of the core-levels Li1s, Nb4s, Nb3d, O1s, and C1s. As expected from majority $LiNbO_3$ phase of each zone, the spectra are representative of $LiNbO_3$ phase,[44,45] and the Li/Nb ratio is found to be equal to the unity, within the instrumental resolution and low signal from the light Li element. No significant changes of the Li/Nb ratio and in chemical shift (Figure S4a, Supporting Information), also of the Nb 3d peaks (Figure 4Sb), have been observed with respect to the different zones of the sample. From the O1s spectra (Figure S4c, Supporting Information), a component appears at higher binding energy (≈532–533 eV), corresponding to surface carbonates and C—O bonds, growing from the Nb-rich zone (Z1) to the Li-rich zone (Z4).[46,47] These observations are consistent with the C1s spectra (Figure S4d, Supporting Information). These surface carbonates could be adsorbed more easily on Li-rich zones.[46,47]

2.3. Structural Characterization

Raman characterization at 633 nm with a lens magnification × 100 has been carried out on C3 and C4 pieces, while Raman characterization at 532 nm (LabRam) has been carried out on piece C2. All spectra are presented in Supporting information in Figure S5 (Supporting Information). Variations of the Raman signal, based on selected spectra of measurements carried out on the zones Z1 to Z6 of C3 piece, are presented in **Figure 7**.

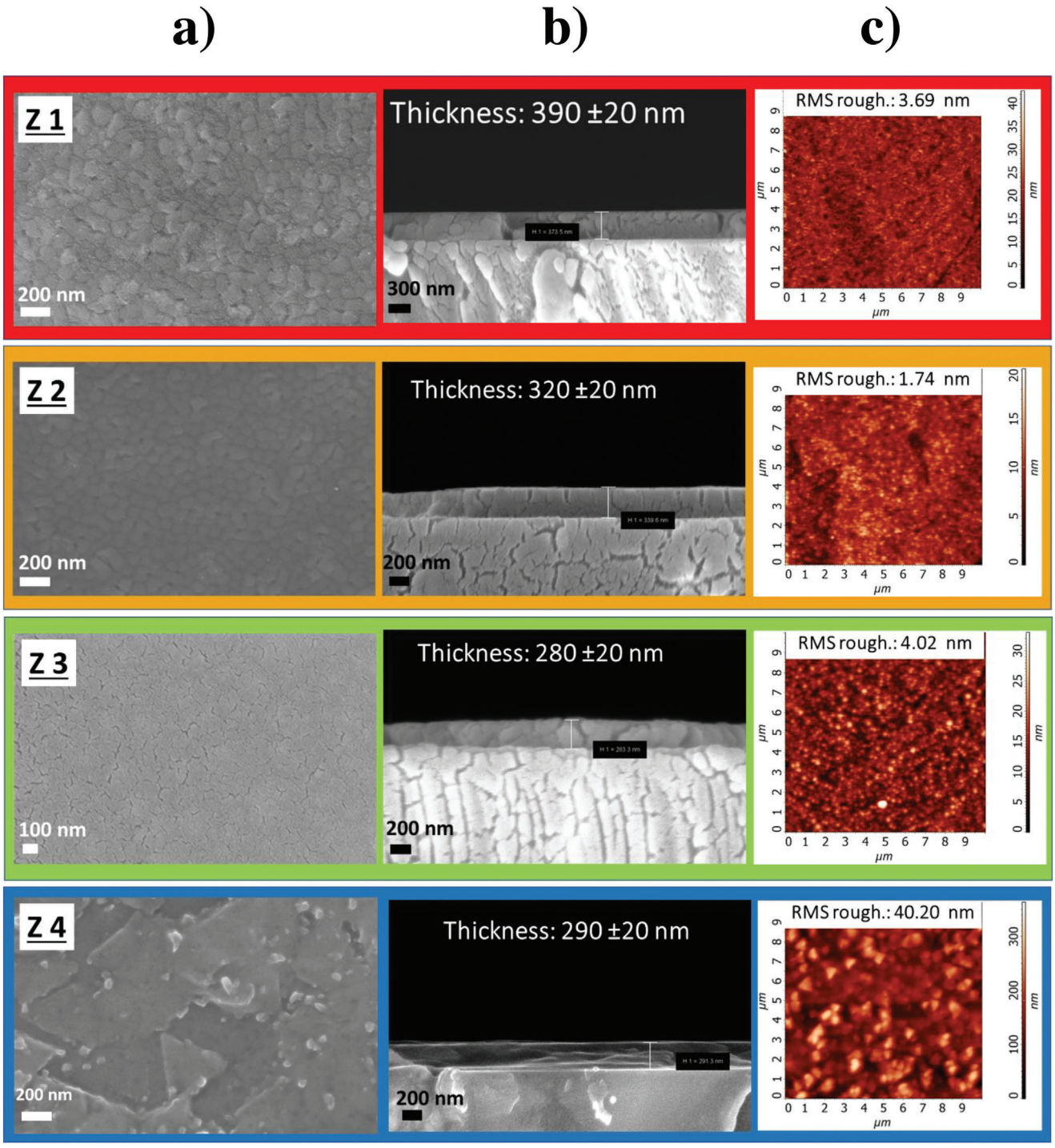

Figure 4. Morphological and topographical characterization of deposited films in zones Z1 to Z4 (according to labelling of Figure S1, Supporting Information): a) FE-SEM plan images and b) cross-sectional images of the deposited films, with estimated film thickness; c) AFM measurements of the film surfaces. RMS roughness values indicated on the images are measured on a 5 × 5 μm^2 area.

Raman spectroscopy is particularly suited to characterize $LiNbO_3$, $LiNb_3O_8$, and Li_3NbO_4 phases, which have a large number of active modes, that can be easily distinguished.[12] In our measurements, the Raman spectra exhibit (in addition to the fine peaks related to the sapphire substrates at 379, 417, 429, 449, 577, and 750 cm^{-1}[48]), standard peaks characteristic of LNO (151, 238, peaks ≈270, peaks ≈325 and 876 cm^{-1}) for zones Z1 to Z4. In Z1, where the Li/Nb precursor flow ratio is the lowest, a peak at 546 cm^{-1} is detected, that is attributed to the Nb rich, $LiNb_3O_8$, phase. In zones Z4 to Z6, peaks at 824 and 905 cm^{-1} are visible,

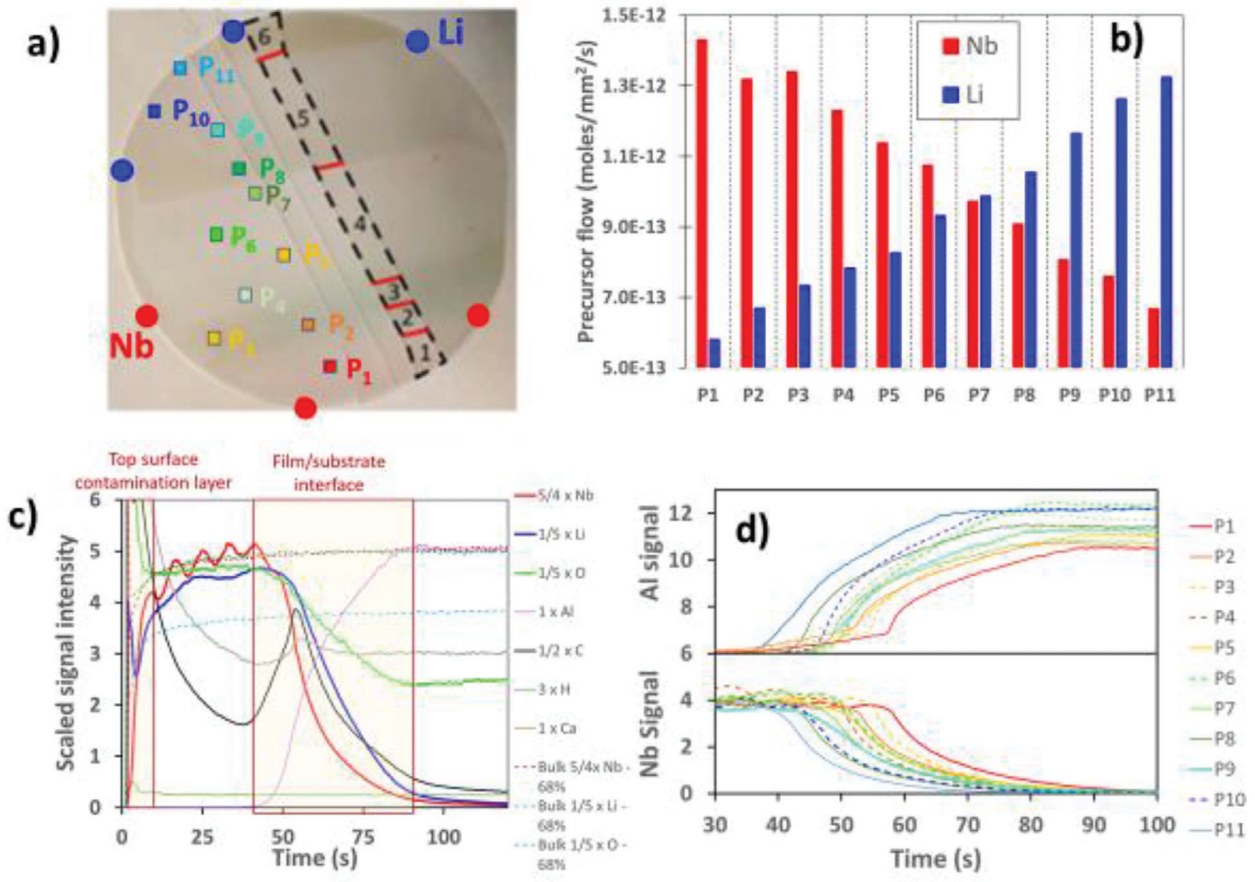

Figure 5. rf-GDOES measurements. a) Wafer photograph with highlighted positions of the 11 measurement points labelled Pi. Dots indicate main direction of flow sources for Li (blue) and Nb (red); b) Flow simulations for Li and Nb precursors at the different measurement points; c) Example of typical rf-GDOES measurement (taken in P5) with different element signals as a function of time, to highlight the main points common to all measurements; measurement on the bulk reference crystal are scaled to 68% and presented as dotted lines for comparison; d) Comparison of the Al signal (from the sapphire substrate) and the Nb signal (from the film) in the measurement time range corresponding to the transition from film to substrate.

that are attributed to Li rich Li_3NbO_4 phase in this Li/Nb high ratio zone (although in the literature the peak at 905 cm^{-1} was attributed to $LiNb_3O_8$[12]). In the intermediary region Z4-Z5, a peak is visible at 625 cm^{-1}, that is also present in Z1 and is compatible with a $LiNb_3O_8$ mode.

If we fit with Lorenzian distribution (Figure S6, Supporting Information), the peaks at respectively 876 cm^{-1} and 153 cm^{-1} (obtained experimentally in our measurements at 869.9 ± 1.9 cm^{-1} see Figure 7c and 151.9 ± 0.7 cm^{-1}, see figure 7b) according to standard relations between peak width and LNO stoichiometry,[49] an average Li content [(%Li)/(%Li+%Nb)] of 51.0 ± 0.6% is estimated, whatever the positions measured in zones Z1 to Z3 (see details in Supporting information, Equation 1). The same data treatment on measurements in Z3 on piece C2 gives a similar Li content of 51.25±0.1% (Figure S6, Supporting Information). Detailed film composition in %Li derived from the experimental width of Raman peaks at 876 and 153 cm^{-1} phonons using Equation 2 and 3, respectively, are reported in Table S1 (Supporting Information).

High-resolution X-ray diffraction (HR-XRD) patterns have been registered at different positions on C3 piece and XRD patterns have also been measured on C1 piece.

HR-XRD diffractograms (**Figure 8**) show that the film in area Z1 to Z4 on C3 piece exhibits, as major peaks, the one for LNO (006) orientation between 38.90° and 39.05°, very close to the bulk value (38.973°), and LNO (00,12) between 83.55° and 83.76° (bulk value at 83.716°), these two orientations belonging to the same crystallographic family plane. In Z2 and Z3 zones, only these LNO (006) and (00,12) are observed, meaning that a pure *c*-axis oriented LNO film is grown. In Z1 area (close to the Nb sources) polycrystalline Nb-rich phase (monoclinic $LiNb_3O_8$) is observed at 19.06° (201 reflection) between 38° and 38.75° (various reflections), at 40.75°, close to the 11–3 reflection, theoretically at 40.814°, and ≈82.6° from higher order reflections. In area Z4, closer to the Li sources, a Li-rich phase, the cubic Li_3NbO_4, is observed. This phase seems to be oriented along the [111] axis, since only hhh reflections are measured, at 36.9° (222), bulk value at 37.02°, and at 78.54°, (444), bulk value at 78.83°, in addition to traces of $LiNb_3O_8$ at ≈40.8°. Zooms on the interesting regions ≈39° and 83°, with assignment of Miller indices to the various peaks, are presented in Supporting Information, Figure S7 (Supporting Information). The 2θ positions of LNO (006) and (00,12) XRD peaks, that increase slightly from Z1 to Z4, imply a decrease of the out-of-plane *c* lattice parameter of ≈0.05 Å with increasing

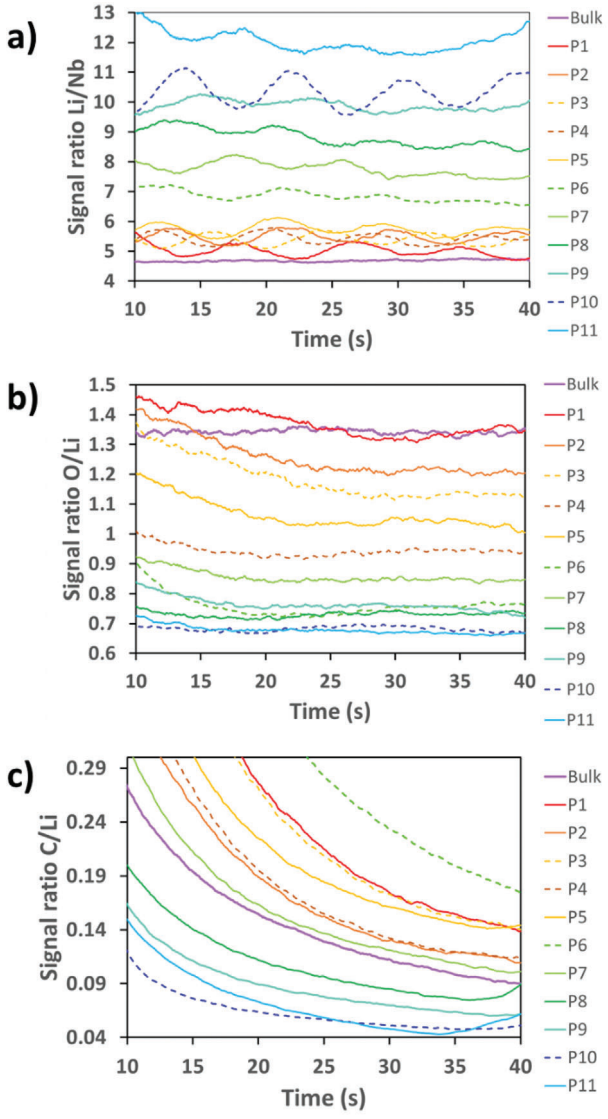

Figure 6. a) Ratio of Li to Nb GDOES signals in the time measurement range corresponding to the deposited film; b) Ratio of O to Li GDOES signals in the time measurement range corresponding to the deposited film; c) Ratio of C to Li GDOES signals in the time measurement range corresponding to the deposited film.

the Li content in the film (from $c = 13.88$ to 13.83 Å), in very good agreement in zone Z2 with theoretical value of 13.86 Å for LNO.

The mosaicity of the layers refers to the slight misorientation of some grains with respect to the others and it is correlated to the width of the rocking curve which gives the spread of these misalignment. The mosaicity has been estimated considering the full width half maximum (FWHM) of rocking curves of LNO (006) at the different positions Z_i (see Figure 7b). The mosaicity is very low in Z2 and Z3, of ≈0.04°, and higher in Z1 (0.32°) and Z4 (1.02°).

The XRD patterns of all the zones from Z1 to Z6 of C2 piece are reported in **Figure 9**. The same findings observed through HR-XRD measurements have been found from Z1 to Z6, with a pure LNO phase in Z2 and Z3. In Z1 the $LiNb_3O_8$ phase is observed, while in the zones Z5 and Z6 the lithium rich phase, namely Li_3NbO_4, is found.

φ-scans and pole figures have been also measured to validate the epitaxial quality of the layers in Z3 (and Z1 for comparison) (**Figure 10**). Pole figures have been recorded for the 012 reflection at $2\theta = 23.63°$.

The epitaxial quality is clearly better in Z3 than in Z1, with less signal out of the poles. In both zones, pole figures and φ scans present a threefold rotational symmetry with 60° rotational domains, evidence of in-plane twins in the LNO films.[30] According

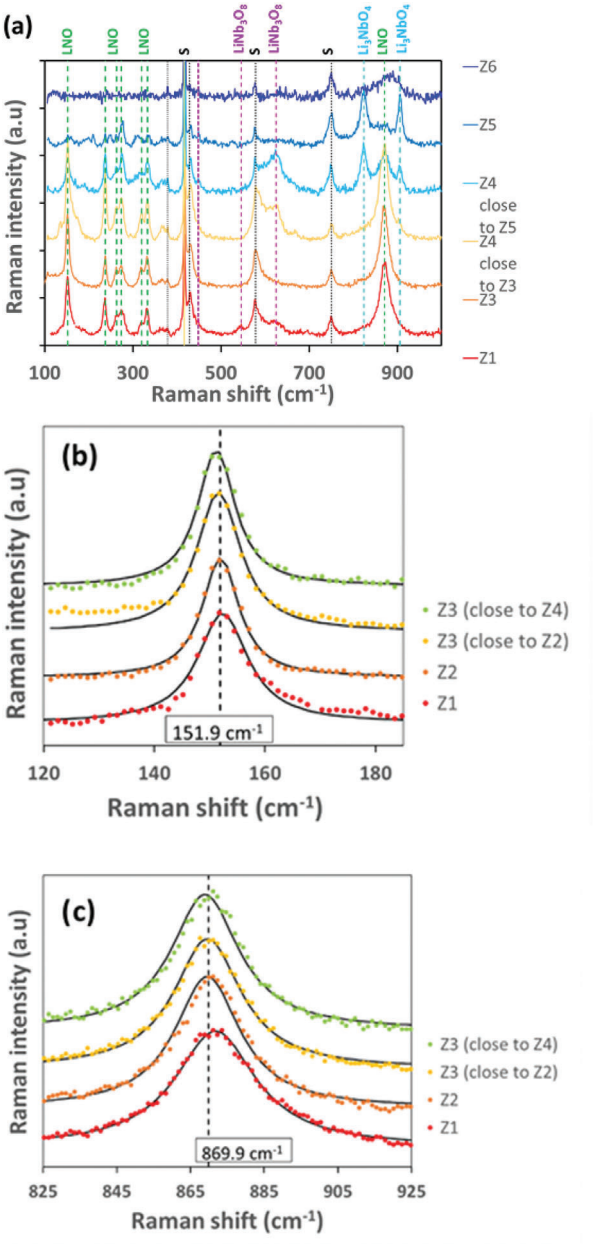

Figure 7. a) Raman spectra (Labram at 532 nm) recorded at different positions in the different zones, decreasing the Li/Nb ratio in precursor flow from Z1 to Z6. b) Zoom on the modes ≈150 cm^{-1} and c) E(1TO) mode ≈870 cm^{-1}.

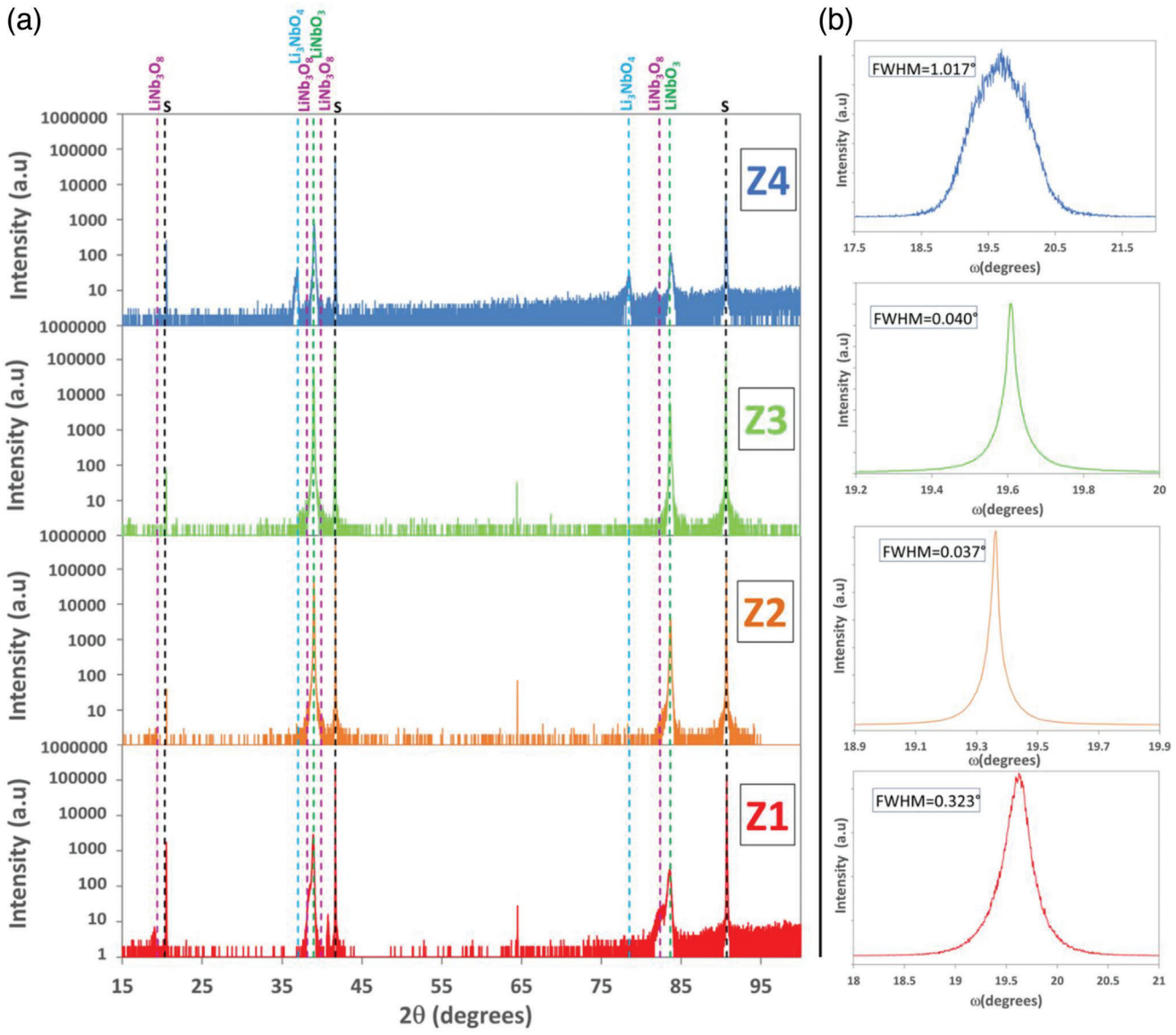

Figure 8. a) Full scale HR-XRD data from $2\theta = 15$ ° to 100° in areas Z1 to Z4 of C2 piece. b) Corresponding rocking curves on LNO (006) at different position from Z1 to Z4 (from bottom to top). For sample identification and position in the wafer see Figure S1 (Supporting Information).

to their relative area on the φ-scan (calculated by fitting all peaks as gaussian) twin crystals are present respectively at 33% for Z1 sample and 13% for Z3 sample, supporting that the best growth conditions are achieved in region Z3. The epitaxial relationship, determined by φ scans shown in Figure 10, of the LNO film on sapphire substrates is $<0001>_{LNO} \parallel <0001>_{Al2O3}$ and $<1010>_{LNO} \parallel <1010>_{Al2O3}$.

2.4. Optical Properties

Film band gap was studied by UV-vis spectroscopy (see Figure S8, Supporting Information).[50] Tauc plot representation to evaluate direct and indirect optical bandgap are shown in **Figure 11**.

No clear-cut description is available in the literature in regard to the LNO optical band gap. Ab-initio calculations proved that the LNO band gap is slightly indirect, with calculated values ranging from 3.5 to 4.7 eV, in function of the used computational methods.[51,52]

Experimental literature data report both direct and indirect band gaps, whose values are strictly related to the material form, single crystal or film, quality, composition, and strain.[53–58] For example, for the single crystal a direct band gap of ≈3.9 eV has been reported for the congruent LNO (CLNO), while a direct bandgap of 4.1 eV has been reported for the near stoichiometric LNO (NSLNO).[53,54] The indirect band gap for the CLNO and NSLNO of single crystals is ≈3.7 and 3.9, respectively.[53,54]

In the case of thin films, direct band gap values ranging from 3.7 to 4.7 eV and indirect band gap values ranging from 3.2 to

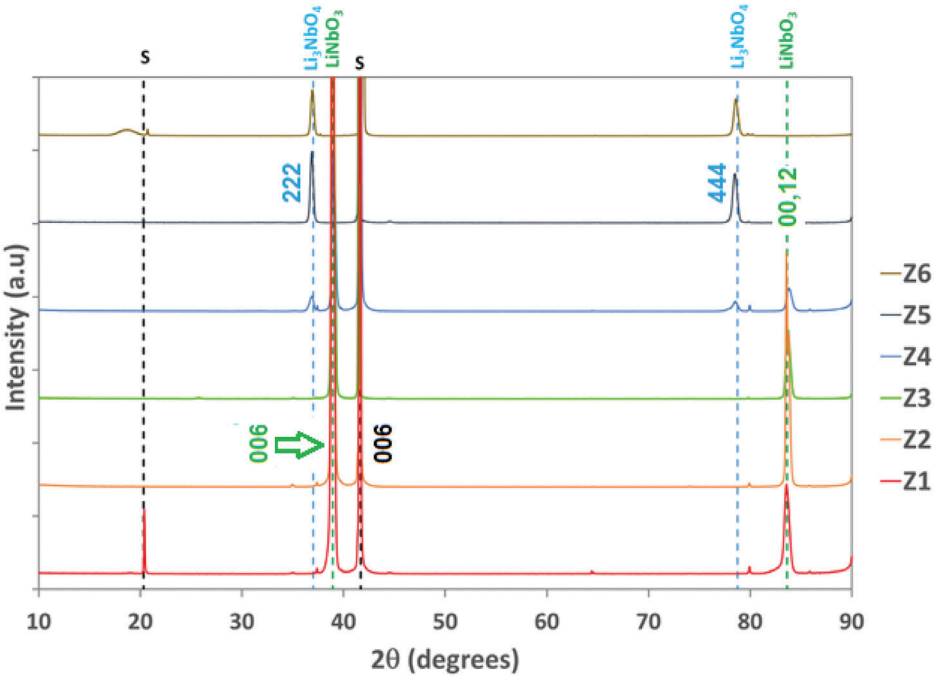

Figure 9. XRD data on C2 part at different positions from Z1 to Z6 (from bottom to top).

4.1 eV have been found depending on the synthetic procedure, i.e., sputtering, laser ablation, sol-gel, etc.[55–58]

Within the literature plethora of data on both direct and indirect band gap of LNO, we have evaluated in our sample both possibilities. In part C2 sample, direct band gap values of 4.39 and 4.60 eV are found for the zones Z2 and Z3, respectively, while the indirect band gap values are 3.85 and 4.25 eV for the Z2 and Z3, respectively. Both assumptions are reliable for our layers since the values perfectly align with literature data of direct and indirect bandgap values.

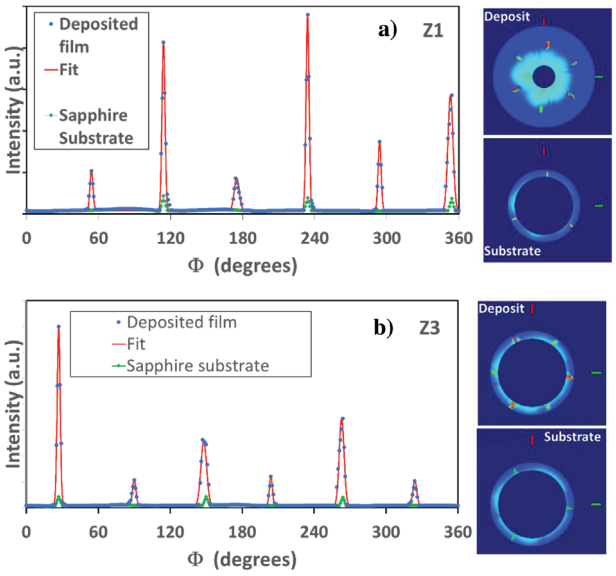

Figure 10. Pole figures and φ-scans measured in Z1 and Z3 of piece C1. Both film and substrate measurements are presented, with in red the experimental fit of the data with Gaussian peaks to estimate proportion of in plane twins. a) For area Z1: $2\theta = 23.63°$ for the film and 25.65° for the substrate, χ range 0–70° and 26–38° for the film and the substrate, respectively. The φ-scan is taken at χ 32°. b) For area Z3: $2\theta = 23.63°$ for the film and 25.65° for the substrate, χ range 26–38°. The φ-scan is taken at χ 32°.

Optical indices n and k have been estimated through ellipsometric measurements carried out every 2 mm along the gradient. At Z2-Z3, the refractive index n for both samples is in the range between 2.18 and 2.24 for 1550 nm wavelength, which is close to the refractive index of the congruently grown LNO.[59]

In Z2-Z3 regions (**Figure 12**a), the refractive index n values are also in very good agreement with reference values for $LiNbO_3$ crystals ≈2.2 at 1500 nm[54] and absorption is very low. Representation of the absorption data in Tauc plot, assuming an indirect band gap, gives a bandgap ≈4.15 eV (Figure 12b). Although optical data fitting might not be optimal due to material property variation, gradual variations of the optical properties seem to be obtained along the precursor flow composition gradient (see for instance n value at 1500 nm in Figure 12c).

Due to the gradual change of Li/Nb ratio on the sample and non-uniform roughness, the model approximation was difficult to perform for the zones Z4-Z6 of the sample C1 (Figure S9, Supporting Information). The measurement showed the variation of the optical dispersion from 1.97 to 2.24 at telecom wavelengths for the zones Z1-Z6 on the sample C4.

2.5. M-line Measurements in $LiNbO_3$ Layers

LNO waveguides are very promising in integrated optics.[60,61] However, as previously indicated in the introduction, growing high quality epitaxial stoichiometric LNO films is still

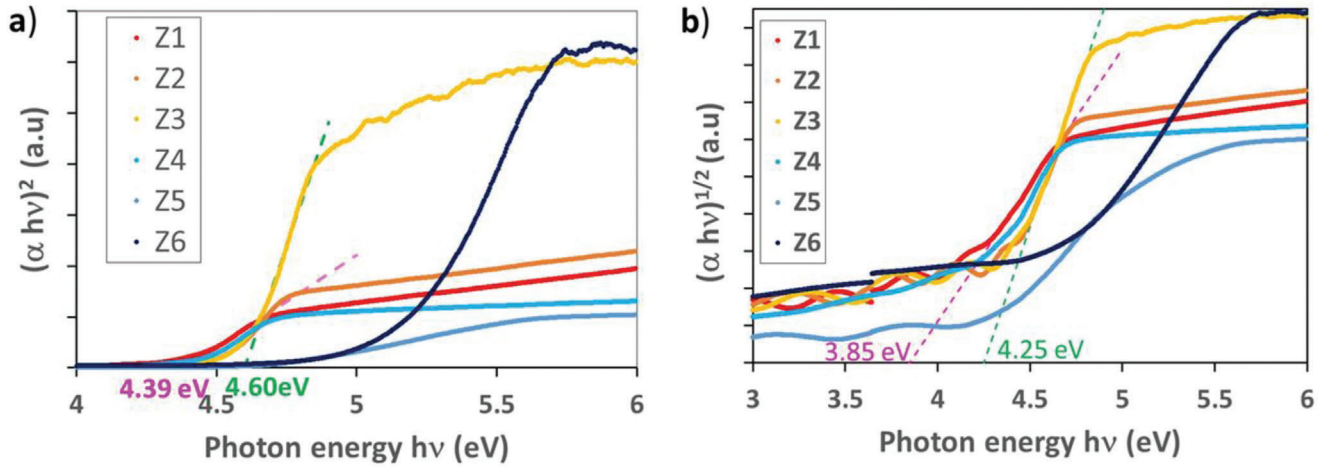

Figure 11. Tauc plots based on UV-vis measurements in the different zones Z1 to Z6 for a) direct and b) indirect bandgap of part C2.

challenging. Therefore, the control of the light propagation in our layers is highly needed to extend the possibility of these layers to photonics applications. For this purpose, we have performed M-line measurements. M-line measurements have been performed in sample piece C1, using TiO_2 high 2.97 refractive index isosceles prism coupler and a 543 nm polarized light source. For sub lambda-air gap between the film and the prism, evanescent coupling can be achieved for critical insertion angles. Such angle has been then incremented up to detecting a guided mode in the thin film giving a black fringe in the output light. Knowing the mode related coupling angles, the effective refractive index of each mode can be obtained.[62] **Figure 13**a shows an example of a Transverse Magnetic (TM) light intensity profile retrieved by the camera (extracted from the measured image in the inset of the Figure) with ɵ the angle between the input beam and the insertion plane prism normal. For this sample the middle fringe corresponding to the guided mode is detected at −7.8°. Measured angles and deduced refractive index for Z2 and Z3 regions for C1 sample extracted from M-line method are reported in Table S2 (Supporting Information). Figure 13b presents the TE and TM modes simulated using SIIO solver[63] on sapphire substrate (1.77 refractive index), corresponding to the measurement presented on the Figure 13a (sample C1, zone Z2). Light is obviously mainly confined in the $LiNbO_3$ layer since its refractive index is higher than the substrate's one.

The different regions of sample C1 (see Figure S1) were measured with M-line. Only zones Z2 and Z3 showed light monomode propagation for both TE and TM polarization, which confirms that zones Z2 and Z3 have very high quality, as previously indicated by the XRD measurements (Figure 8 and 9). Such measurements confirm once again that the region of interest is at ≈0.5 Li Nb^{-1} flow ratio. Using the thickness determined through FE-SEM cross-sections (Figure 4), a refractive index of 2.27 ± 0.03 is found for both regions and polarization in relatively good agreement with ref.[59 and the ellipsometry measurements (details in Supporting Information). These results demonstrate that $LiNbO_3$ thin films are capable of guiding light and that further optical experiments can be made. Thus, this last result opens perspectives to our method in integrated optics.

3. Discussion

The deposited thin films achieved with a variable Li/Nb precursor flow ratio from 0.25 to 2.45 (see Figure 3) demonstrate that this parameter is critical for the film properties, and that the best film properties with the ambition of depositing stoichiometric and epitaxial *c*-axis oriented LNO films are only obtained for a narrow range of this ratio (typically for Li/Nb precursor flow in the range 0.4 to 0.6). This result is in perfect agreement with estimation reported in a previous study,[18] that gave a value between 0.485 and 0.583, (normalizing by the factor 6 taken in[18] for the assumed hexameric nature of the $[Li(OtBu)]_6$ precursor not taken into account in this work).

In these conditions, XRD diffractograms (see Figure 8 and 9) only exhibit LNO peaks for the *c*-axis oriented (respectively 006 and 00,12 reflections) and rocking curves of the (006) peak demonstrate a very low mosaicity of ≈0.04° (lower value of 0.0295° was previously obtained by CBVD but for a thinner film of 150 nm instead of ≈300 nm as in the present work). The epitaxial quality presently obtained for *c*-axis oriented LNO growth on sapphire is similar to the best reported by other CVD techniques (mosaicity of 0.044°[40]), that are usually better than for thin films obtained by other deposition techniques (0.35° by PLD,[26] 0.76° by sol gel[27] for instance), except by MBE, 0.0024°[25b] obtained, however, at much lower growth rates, temperatures higher than 1000 °C and for very small film thickness (<60 nm).

Raman spectroscopy confirms the nature of the crystalline phase, and Raman peak width analysis demonstrates that films are slightly Li rich (51 ± 0.6%). FE-SEM and AFM analyses evidence a homogenous granular structure of the film with a very low RMS roughness (less than 2 nm).

In our experiment, at smaller Li/Nb precursor flow ratios than the optimized condition, $LiNb_3O_8$ (Nb rich phase) is evidenced by both Raman and XRD, while at higher Li/Nb precursor flow ratios, the Li_3NbO_4 (a Li rich phase) is observed, in good agreement with other deposition studies by CVD techniques.[9,19]

All the characterizations carried out to screen precursor flow conditions to optimize LNO properties are time consuming, and it is interesting to see how the obtained properties correlate with the very rapid rf-GDOES analysis (**Figure 14**). In the present

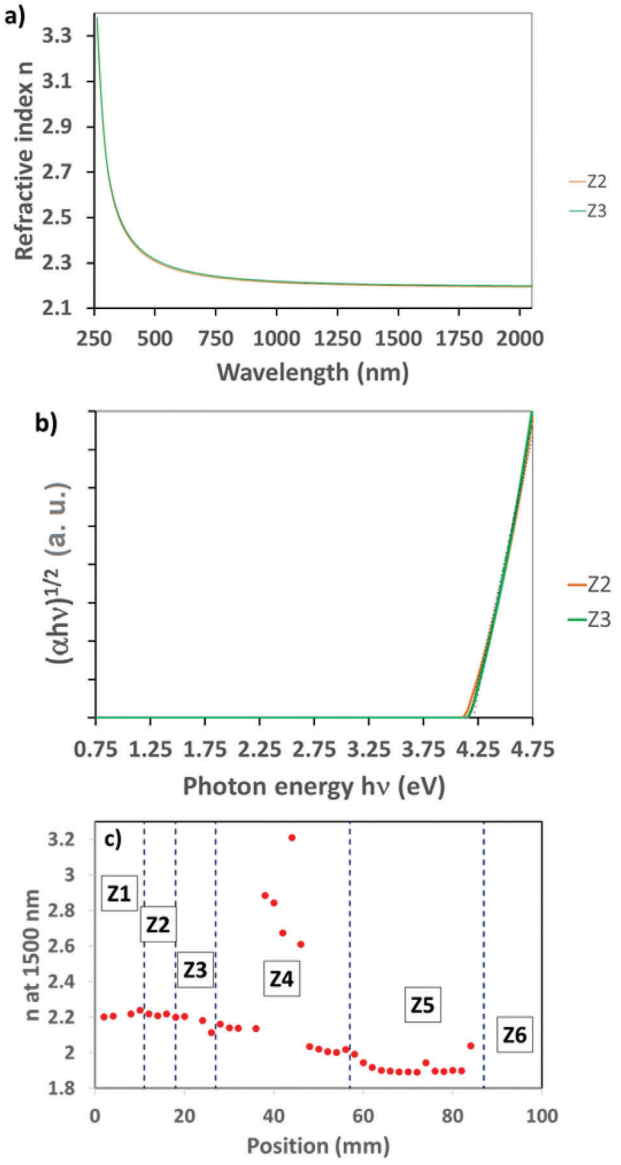

Figure 12. a) Refractive index n and b) indirect Tauc's plot, both in Z2. c) n value as a function of position in zone C1.

work, GDOES data have been analyzed with respect to the film measurement point P1 for which GDOES signals are very close to the bulk LNO reference crystal which is assumed to be stoichiometric. Composition has been estimated assuming linearity of the signal with the element content (Figure SS4, Supporting Information).

It is observed that whatever the Nb precursor flow value, the Nb film content remains quite constant (red points and dotted line in Figure 14), while the Li content (blue point and dotted line) increases almost linearly with the Li/Nb flow ratio. Thus, based on the calibration, the best film properties are achieved for slightly Li rich films (in agreement with Raman observations) in zones Z2 and Z3. What is particularly interesting is that the O signal seems to be a good indicator of the best film composition: it seems to exhibit a minimum at this best precursor flow composition, while the presence of contamination phases $LiNb_3O_8$ (at lower Li/Nb) and Li_3NbO_4 (at higher Li/Nb) both induce an excess of O with respect to $LiNbO_3$.

Additionally, erosion time, till the Nb to Al signals transition is reached, seems to be a good indicator of film thickness, as it is in qualitative agreement with FE-SEM cross-sectional measurements. Growth rate achieved in the best epitaxial area is of the order of 75 nm h^{-1}. This value is a little bit low in comparison to an estimated growth rate that would be obtained in mass transfer limited regime assuming all precursor above limiting flow for Li or Nb leads to deposition of $LiNbO_3$: ≈120 nm h^{-1} (or assuming all Nb precursor leads to $LiNbO_3$ without Li(OtBu) being oligomerized, ≈195 nm h^{-1}). This confirms that the mechanism is complex and possibly with auto-limiting steps as studied with similar conditions in analogous high vacuum CVD conditions.[29]

The cracks observed by optical microscopy have already been reported in literature for LNO growth on sapphire substrate by MOCVD for films thicker than 150 nm and have been attributed to tensile stresses developing during cooling due to the almost double thermal expansion coefficient of LNO with respect to sapphire at 25 °C.[40,64] They are reported even for the best epitaxial LNO thin films obtained by MBE with a low mosaicity.[25b]

The presence of in-plane twins, observed in the φ-scan, has been reported in numerous literature reports on LNO thin film deposition.[30] They have been shown to be substrate temperature dependent, and can be removed depositing at higher temperature or by post deposition annealing.[40] For example, no twins have been found in MBE deposited films at 1000 °C.[25b]

4. Conclusion

Very high-quality LNO films have been deposited through a combinatorial high vacuum chemical beam vapor deposition by varying the Li/Nb precursor flow ratios. The study has allowed to determine the suited Li/Nb flow ratio to produce high epitaxial quality LNO films in a less time-consuming approach than classical vapor phase routes, either chemical or physical. rf-GDOES has been applied for the first time, to our knowledge, as a very rapid and efficient way of screening film composition as a function of Li/Nb ratio.

These findings confirm the potentiality of CBVD to optimize growth of high epitaxial quality LNO films. The presented approach is easily scalable to mass production as deposition has been already demonstrated for substrates of 450 mm in diameter for other materials.[35,65]

Further film improvement will be investigated in next experiments by exploring lower deposition temperatures (below 450 °C) with further recrystallization either by rapid thermal annealing or by laser assisted or post-deposition irradiation.

Finally, results obtained in the combinatorial mode envisage the fabrication of homogenous LNO samples replicating on full wafers the growth of high-quality epitaxial LNO films following a modified procedure of the presently applied.

5. Experimental Section

Precursors: Lithium tert-butoxide ($[Li(OtBu)]_6$, CAS 1907-33-1, was purchased from STREM with a purity of 98%. Niobium tetraethoxide

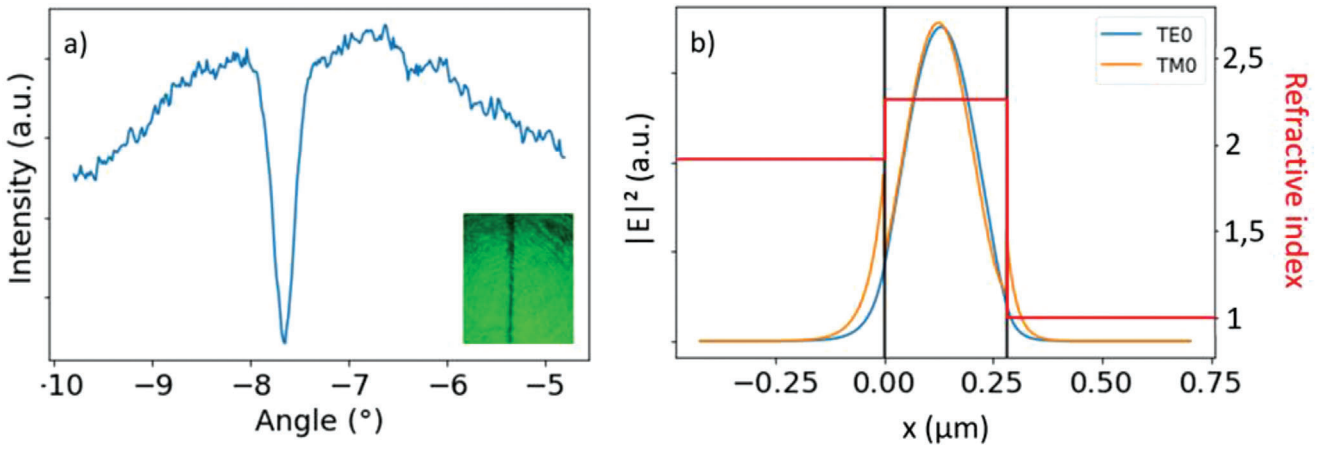

Figure 13. a) A pattern image with extracted intensity profile of a TM guided mode on sample part C1, zone Z3 by the M-line method with the b) corresponding calculated electromagnetic field and refractive index of the stacking for the measured mode.

dimethylaminoethoxide [$Nb(OEt)_4$dmae], CAS 359847-15-7, was synthesized following a modified procedure based on Timothy Leedham's and John Drake's patent.[66,67] Details of the synthesis was reported in the supporting information.

Growth Conditions: Lithium tert-butoxide ($[Li(OtBu)]_6$ and niobium tetraethoxide dimethylaminoethoxide ($Nb(OEt)_4$dmae were evaporated independently from thermostated reservoirs (at respectively 95.4 ± 0.2 °C and 67.7 ± 0.7 °C, resulting in measured pre-chamber pressures of respectively 13.1 ± 0.4 10^{-3} mbar and 30.2 ± 1.6 10^{-3} mbar). Growth was carried out in a Sybilla deposition equipment from ABCD Technology[32] for 150 mm wafers with 3 independent precursor lines (see system principle in **Figure 15**, and more precise description in[33]).

The 4-inch sapphire substrate (from Cryscore Optoelectronic Limited) was radiatively heated to 650 °C from a graphite plate at 773 ± 3 °C and the main chamber pressure was maintained below 7×10^{-5} mbar. Precise deposition parameter variation and stability over time were presented in Supporting Information Figure S10, Supporting Information). Growth was carried out for 4 h to obtain film thickness of ≈300 nm (growth rate of ≈75 nm h^{-1}).

Characterization Techniques–GDOES: The GD measurements were done on a GD Profiler 2 (Horiba France) equipped with DIP, differential interferometry profiling tool. Operating conditions were 750 Pa and 25 W in pulsed operation mode at 111 Hz and duty cycle 0.3 with synchronized acquisition. Elements of interest were measured at their most sensitive wavelengths Li 670.8 nm, Al 396.15 nm, Nb 316.34 nm, O 130.22 nm.

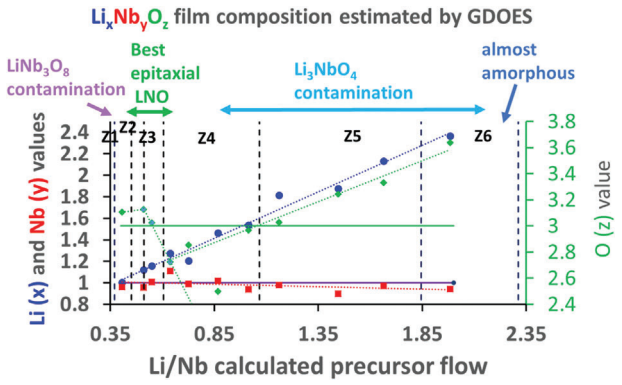

Figure 14. Film composition estimated by GDOES normalizing linear signal from calibration of signals on bulk crystal in function of Li/Nb calculated precursor flow. The blue, red, green full lines indicate the stoichiometric amount of Li, Nb, and O, respectively, in the $LiNbO_3$ bulk, while the dotted lines indicate the experimental trend in the deposited wafer.

Characterization Techniques–XPS Measurements: The chemical analysis of the surface region has been performed on the film C2 (on three different zones) by X-ray photoelectron spectroscopy (XPS) from the core level spectra (Li1s, Nb4s, Nb3d, O1s, and C1s) at normal emission with Al K_α photon source energy at 1486.6 eV.

Characterization Techniques–XRD/HR-XRD/Rocking Curves/Pole Figures: XRD analyses were used to investigate the phases, structure and the crystalline orientation of the film at different zones. Patterns were recorded in Bragg-Brentano geometry using a Smartlab Rigaku diffractometer operating at 45 kV and 200 mA equipped with a rotating anode of Cu K_α (1.5418 Å) radiation. High resolution XRD patterns were recorded using the Rigaku SmartLab equipped with a two-bounces Ge (220) monochromator (λ Cu $K_{\alpha 1}$ = 1.54056 Å). Rocking curves were recorded for the 006 reflection using the same diffractometer. Pole figures were recorded for the 012 reflection at $2\theta = 23.63°$ in the χ range 0–70°. The φ-scan was taken at χ 32°.

Characterization Techniques–FE-SEM: Film morphologies were investigated using the field emission scanning electron microscope (FE-SEM) ZEISS SUPRA 55 VP. All the samples deposited on sapphire were Au-coated through sputtering before FE-SEM analyses to improve the image resolution without altering the system morphology since only few nanometer were used. Images were recorded at 15 keV electron beam and with a working distance in the 2.8–4 mm range.

Characterization Techniques–AFM: Topographic characterization was performed through Atomic Force Microscopy (AFM) using the NT-MDT SPM apparatus. The images were obtained in contact mode, adopting an Au coated silicon probe with a nominal 35 nm tip curvature radius and a typical force constant of 0.1 N. The noise level was 0.01 nm before and after each measurement. The NOVA software was used for the RMS roughness evaluation.

Characterization Techniques–UV-vis: The UV-Visible absorption spectra were recorded using a Jasco V-650 spectrophotometer. The spectra were recorded in the wavelength range from 200 to 800 nm for LNO-thin films deposited on sapphire substrates.

Characterization Techniques–Raman: The samples were probed using Raman spectroscopy to have access to their vibrational modes and indirectly to their crystalline order. Two set-ups were used. The first one was a Horiba LabRAM HR evolution with a 532 nm laser source, an 1800 grove mm^{-1} providing a spectral resolution of 1 cm^{-1} and a lateral spatial resolution of 0.6 µm. The power of the excitation lasers at both setups was no larger than 10% of maximum to ensure no photodegradation of the samples. The second setup was Renishaw inVia^{TM} with a laser of 633 nm which provides spectral resolution of 0.3 cm^{-1} and a lateral spatial resolution of 0.25 µm.

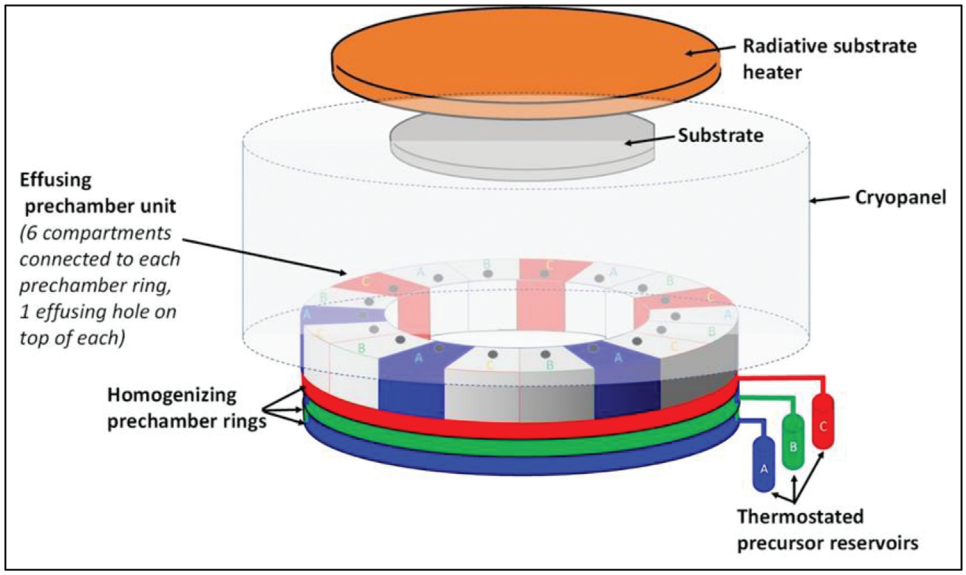

Figure 15. Schematic of the CBVD system Sybilla 150 from ABCD Technology used in the present studies. The system includes three independent lines of precursor delivery (labelled A, B, and C): each precursor is evaporated from a thermostated reservoir into a homogenizing pre-chamber ring, which is connected on its top to 6 independent volumes, on top of which the molecules effuse into the main chamber maintained in high-vacuum, both by the action of a turbomolecular pump and of surrounding cryo-panel maintained at liquid nitrogen temperature. The precursor molecules reach the substrate with line-of-sight trajectories from the Knudsen holes, and decompose thermally on it (due to the radiative heating of the substrate). In the present study, Li precursor was placed on line A, and the 3 pre-chamber sources colored in blue were open, while the Nb precursor was placed on line C and the 3 pre-chamber sources colored in red were open. The precursors effused from the pre-chamber to the substrate through Knudsen holes (3 for each precursor line positioned at 60° on the source ring and in opposite directions for the two precursors, to generate a continuous gradient of precursor ratio along the substrate).

Characterization Techniques–Ellipsometry: Measurements of the complex refractive index were carried out using a Horiba Jobin Yvon spectroscopic ellipsometer. The wavelength range of the light source goes from 250 nm to 2100 nm. The configuration of the ellipsometer setup was light source-polarizer-sample-analyser-detector with the angle of incidence set at 70°. The complex dielectric functions of the thin films of $LiNbO_3$ and their thicknesses can be derived by fitting realistic optical models to the experimental data. To model the sample under study, a three-layer model was used including, from bottom to top, the sapphire substrate and the lithium niobate layer (both modelled with a Tauc-Lorentz dispersion) and a roughness layer on the surface (modelled as an effective medium mixing $LiNbO_3$ and air).

Characterization Techniques–M-Line: Light was coupled into the planar thin film with a prism put on top of the layer. The prism was mounted on a rotatable mount to vary the insertion angle with a camera which retrieves the prism-output figure. The insertion angle was first calibrated using the back reflection corresponding to the zero angle.[55]

Supporting Information

Supporting Information is available from the Wiley Online Library or from the author.

Acknowledgements

A.L.P., F.L.P., and G.M. thank the University of Catania for financial support within the PIACERI research program UNICT 2020–22 Linea 2 and the Bionanotech Research and Innovation Tower (BRIT) laboratory of University of Catania (Grant no. PONa3_00136 financed by the Italian Ministry for Education, University and Research, MIUR) for the diffractometer facility. A.L.P. thanks the Ministero dell'Università e della Ricerca within the PON "Ricerca e Innovazione" 2014–2020 Azioni IV.4 program. M.R. thanks the ECLAUSion project, that has received funding from the European Union's Horizon 2020 research and innovation program under the Marie Sklodowska-Curie grant agreement N° 801512. B.M. is grateful to the CECOMO center for the access to the Horiba LabRAM spectrometer.

Open access funding was provided by Universita degli Studi di Catania within the CRUI-CARE Agreement.

Conflict of Interest

The authors declare no conflict of interest.

Data Availability Statement

The data that support the findings of this study are available in the supplementary material of this article.

Keywords

chemical beam epitaxy, combinatorial, epitaxial films, lithium niobate, optical properties, structural properties

Received: June 22, 2023
Revised: August 8, 2023
Published online:

[1] E. D. K. K. Wong, *Northstar Photonics, Inc. USA, INSPEC, The Institution of Electrical Engineers*, **2002**, London, United Kingdom.

[2] R. S. Weis, T. K. Gaylord, *Appl. Phys. A* **1985**, *37*, 191.
[3] K. Chen, Y. Zhu, Z. Liu, D. Xue, *Molecules* **2021**, *26*, 7044.
[4] V. Bornand, P. H. Papet, *Ferroelectrics* **2003**, *288*, 187.
[5] M. Weiß, H. J. Krenner, *J. Phys. D: Appl. Phys.* **2018**, *51*, 373001.
[6] a) O. Sánchez-Dena, C. D. Fierro-Ruiz, S. D. Villalobos-Mendoza, D. M. Carrillo Flores, J. T. Elizalde-Galindo, R. Farías, *Crystals* **2020**, *10*, 973; b) J. Streque, T. Aubert, N. Kokanyan, F. Bartoli, A. Taguett, V. Polewczyk, E. Kokanyan, S. Hage-Ali, P. Boulet, O. Elmazria, *IEEE Sensors Lett* **2019**, *3*, 2501254.
[7] C. Wang, M. Zhang, X. Chen, M. Bertrand, A. Shams-Ansari, S. Chandrasekhar, P. Winzer, M. Lončar, *Nature* **2018**, *562*, 101.
[8] J. Cai, C. Guo, C. Lu, A. Pak Tao Lau, P. Chen, L. Liu, *IEEE Photonics J* **2021**, *13*, 2200206.
[9] M. Thomaschewski, V. A. Zenin, S. Fiedler, C. Wolff, S. I. Bozhevolnyi, *Nano Lett.* **2022**, *22*, 6471.
[10] M. Manzo, F. Laurell, V. Pasiskevicius, K. Gallo, *Nano-Optics for Enhancing Light-Matter Interactions on a Molecular Scale* (Eds: B. Di Bartolo, Ed., J. Collins), NATO Science for Peace and Security Series B: Physics and Biophysics. Springer, Switzerland, **2013**, Ch. 42.
[11] B. Zivasatienraj, M. B. Tellekamp, W. A. Doolittle, *Crystals* **2021**, *11*, 397.
[12] a) L. C. Sauze, N. Vaxelaire, R. Templier, D. Rouchon, F. Pierre, C. Guedj, D. Remiens, G. Rodriguez, M. Bousquet, F. Dupont, *J. Cryst. Growth.* **2023**, *601*, 126950; b) A. Bartasyte, V. Plausinaitiene, A. Abrutis, S. Stanionyte, S. Margueron, P. Boulet, T. Kobata, Y. Uesu, J. Gleize, *J. Phys.: Condens. Matter.* **2013**, *25*, 205901.
[13] A. Bartasyte, S. Margueron, T. Baron, S. Oliveri, P. Boulet, *Adv. Mater. Interfaces* **2017**, *4*, 1600998.
[14] D. Zhu, L. Shao, M. Yu, R. Cheng, B. Desiatov, C. J. Xin, Y. Hu, J. Holzgrafe, S. Ghosh, A. Shams-Ansari, E. Puma, N. Sinclair, C. Reimer, M. Zhang, M. Lončar, *Adv. Opt. Photon.* **2021**, *13*, 242.
[15] A. Al Sayem, Y. Wang, J. Lu, X. Liu, A. W. Bruch, H. X. Tang, *Appl. Phys. Lett.* **2021**, *119*, 231104.
[16] X. He, K. Chen, L. Kong, P. Li, *Appl. Phys. Lett.* **2022**, *120*, 113507.
[17] S. Shandilya, M. Tomar, K. Sreenivas, V. Gupta, *J. Phys. D: Appl. Phys.* **2009**, *42*, 095303.
[18] A. Dabirian, S. Harada, Y. Kuzminykh, S. C. Sandu, E. Wagner, G. Benvenuti, P. Brodard, S. Rushworth, P. Muralt, P. Hoffmann, *J. Electrochem. Soc.* **2011**, *158*, D72.
[19] O. Sánchez-Dena, C. J. Villagómez, C. D. Fierro-Ruíz, A. S. Padilla-Robles, R. Farías, E. Vigueras-Santiago, S. Hernández-López, J.-A. Reyes-Esqueda, *Crystals* **2019**, *9*, 340.
[20] Y. Lu, B. Johnston, P. Dekker, M. J. Withford, J. M. Dawes, *Molecules* **2020**, *25*, 3925.
[21] L. C. Sauze, N. Vaxelaire, D. Rouchon, F. Pierre, R. Templier, D. Remiens, G. Rodriguez, *J. Vac. Sci. Technol. A* **2020**, *38*, 043205.
[22] J. A. Ocón, J. G. Murillo, M. Miki-Yoshid, M. N. Cardoza, O. E. Contreras-López, *J. Crystal Growth* **2014**, *408*, 64.
[23] M. Kadota, Y. Suzuki, Y. Ito, *Jap. J. Appl. Phys.* **2011**, *50*, 07HD11.
[24] a) Z. Vakulov, D. Khakhulin, A. Geldash, R. V. Tominov, V. S. Klimin, V. A. Smirnov, O. A. Ageev, *J. Adv. Dielec.* **2022**, *12*, 2160019; b) S. Kilburger, E. Millon, P. Di Bin, A. Boulle, R. Guinebretière, C. Di Bin, *Thin Solid Films* **2010**, *518*, 4654.
[25] a) M. B. Tellekamp, J. C. Shank, W. A. Doolittle, *J. Crystal Growth* **2017**, *463*, 156; b) M. B. Tellekamp, J. C. Shank, M. S. Goorsky, W. A. Doolittle, *J. Electr. Mater.* **2016**, *45*, 6292.
[26] a) V. Mereacre, J. R. Binder, *Inorg. Chem.* **2022**, *61*, 7222; b) T. A. Derouin, C. D. E. Lakeman, X. H. Wu, J. S. Speck, F. F. Lange, *J. Mater. Res.* **1997**, *12*, 1391.
[27] E. Østreng, H. H. Sønsteby, T. Sajavaara, O. Nilsen, H. Fjellvåg, *J. Mater. Chem. C* **2013**, *1*, 4283.
[28] W. T. Tsang, *J. Crystal Growth* **1991**, *111*, 529.
[29] Y. Kuzminykh, A. Dabirian, M. Reinke, P. Hoffmann, *Surf. Coat. Technol.* **2013**, *230*, 13.
[30] A. Dabirian, Y. Kuzminykh, S. C. Sandu, S. Harada, E. Wagner, P. Brodard, G. Benvenuti, S. Rushworth, P. Muralt, P. Hoffmann, *Crystal Growth Design* **2011**, *11*, 203.
[31] J. Malherbe, B. Fernández, H. Martinez, P. Chapon, P. Panjan, O. F. X. Donard, *J. Anal. At. Spectrom.* **2008**, *23*, 1378.
[32] ABCD Technology – Basics for a New Start!, ABCD Technology. (n.d.) https://abcdtechnology.com/ (accessed March 2020).
[33] E. Wagner, C. S. Sandu, S. Harada, C. Pellodi, M. Jobin, P. Muralt, G. Benvenuti, *ACS Combinat. Sci.* **2016**, *18*, 154.
[34] A. Dabirian, Y. Kuzminykh, E. Wagner, G. Benvenuti, S. Rushworth, P. Hoffmann, *Thin Solid Films* **2014**, *571*, 94.
[35] E. Wagner, W. Maudez, S. Bagdzevicius, C. S. Sandu, G. Benvenuti, in: *Oxide-Based Materials and Devices XII, International Society for Optics and Photonics*, **2021**: 116871Z.
[36] G. Benvenuti, E. Halary-Wagner, A. Brioude, P. Hoffmann, *Thin Solid Films* **2003**, *427*, 411.
[37] E. Wagner, C. S. Sandu, S. Harada, G. Benvenuti, V. Savu, P. Muralt, *Thin Solid Films* **2015**, *586*, 64.
[38] D. Saulys, V. Joshkin, M. Khoudiakov, T. F. Kuech, A. B. Ellis, S. R. Oktyabrsky, L. McCaughan, *J. Crystal Growth.* **2000**, *217*, 287.
[39] J. D. Kahn, A. Haag, P. v. R. Schleyer, *J. Phys. Chem.* **1988**, *92*, 212.
[40] R. S. Feigelson, *J. Crystal Growth.* **1996**, *166*, 1.
[41] S. Sanna, W. G. Schmidt, *J. Phys.: Condens. Matter.* **2017**, *29*, 413001.
[42] L. Niobate, (LiNbO3) Substrates for Photonics Research, 2018, https://www.universitywafer.com/lithium-niobate-linbo3.html(accessed: June 2022).
[43] L. Therese, Z. Ghalem, P. Guillot, P. Belenguer, *Anal. Bioanal. Chem.* **2006**, *386*, 163.
[44] E. A. Skryleva, I. V. Kubasov, P.h.V. Kiryukhantsev-Korneev, B. R. Senatulin, R. N. Zhukov, K. V. Zakutailov, M. D. Malinkovich, Y.u. N. Parkhomenko, *Appl. Surf. Science* **2016**, *389*, 387.
[45] M. Aufray, S. Menuel, Y. Fort, J. Eschbach, D. Rouxel, B. Vincent, *J. Nanoscience and Nanotechnology* **2009**, *9*, 4780.
[46] F. Walther, F. Strauss, X. Wu, B. Mogwitz, J. Hertle, J. Sann, M. Rohnke, T. Brezesinski, J. Janek, *Chem. Mater.* **2021**, *33*, 2110.
[47] N. Hornsveld, B. Put, W. M. M. Kessels, P. M. Vereecken, M. Creatore, *RSC Adv.* **2017**, *7*, 41359.
[48] M. Kadleıḱová, J. Breza, M. Veselý, *Microelectronics J* **2001**, *32*, 955.
[49] U. Schlarb, S. Klauer, M. Wesselmann, K. Betzler, M. Wöhlecke, *Appl. Phys. A.* **1993**, *56*, 311.
[50] P. Y. Yu, M. Cardona, *Fundamentals of semiconductors*, Springer, Berlin, Germany, **1996**.
[51] S. Mamouna, A. E. Merad, L. Guilbert, *Comput. Mater. Sci.* **2013**, *79*, 125.
[52] C. Thierfelder, S. Sanna, A. Schindlmayr, W. G. Schmidt, *Physica Status Solidi C* **2010**, *7*, 362.
[53] R. Bhatt, S. Ganesamoorthy, I. Bhaumik, A. K. Karnal, P. K. Gupta, *J. Phys. Chem. Solids* **2012**, *73*, 257.
[54] R. Bhatt, I. Bhaumik, S. Ganesamoorthy, A. K. Karnal, M. K. Swami, H. S. Patel, P. K. Gupta, *Physica Status Solidi A* **2012**, *209*, 176.
[55] A. Tumuluria, M. S. S. Bharatia, S. Venugopal Raoa, K. C. James Rajua, *Mater. Res. Bulletin* **2017**, *94*, 342.
[56] M. A. Fakhri, E. T. Salim, M. H. A. Wahid, U. Hashim, Z. T. Salim, R. A. Ismail, *J. Mater Sci: Mater Electron.* **2017**, *28*, 11813.
[57] M. Sumetsa, O. Ovchinnikov, V. Ievlev, A. Kostyuchenko, *Ceram. Int.* **2017**, *43*, 13565.
[58] S. Satapathy, C. Mukherjee, T. Shaktawat, P. K. Gupta, V. G. Sathe, *Thin Solid Films* **2012**, *520*, 6510.
[59] D. E. Zelmon, D. L. Small, D. Jundt, *J. Opt. Soc. Am. B* **1997**, *14*, 3319.
[60] Y. Zheng, X. Chen, *Adv. in Physics: X* **2021**, *6*, 1889402.
[61] M. Churaev, R. N. Wang, A. Riedhauser, V. Snigirev, T. Blésin, C. Möhl, M. H. Anderson, A. Siddharth, Y. Popoff, U. Drechsler, D. Caimi, S. Hönl, J. Riemensberger, J. Liu, P. Seidler, T. J. Kippenberg, *Nat. Commun.* **2023**, *14*, 3499.

[62] J. E. Batubara, H. R. Yulianto, H. P. Uranus, M. Muljono, Design, Fabrication, and Characterization of Photonic Devices in *International Symposium on Photonics and Applications*, **1999**, *3896*, Singapore.
[63] OMS, 1-D mode solver for dielectric multilayer slab waveguides – Simulation in Integrated Optics, https://www.siio.eu. (accessed: June 2023)
[64] A. Bartasyte, V. Plausinaitiene, A. Abrutis, S. Stanionyte, S. Margueron, V. Kubilius, P. Boulet, S. Huband, P. A. Thomas, *Mater. Chem. Phys.* **2015**, *150*, 622.
[65] C. Garlisi, P. Lunca Popa, K. Menguelti, V. Rogé, M. Michel, C. Vergne, J. Guillot, E. Wagner, W. Maudez, G. Benvenuti, B. R. Pistillo, E. Barborini, *Nanomaterials* **2022**, *12*, 1012.
[66] D. Bijou, *PhD thesis Synthesis and characterization of new inorganic molecular precursors for the deposition of multifunctional metal oxide films by CBVD*, **2018**, Ecole Doctorale de Chimie, Lyon.
[67] T. Leedham, S. Drake, Tantalum Compounds, WO9526355 (A1), October 5, 1995, https://worldwide.espacenet.com/publicationDetails/biblio?FT=D&date=19951005&DB=&locale=fr_EP&CC=WO&NR=9526355A1&KC=A1&ND=4 (accessed: June 2023)